JOINT EUROPEAN TORUS JET

JET–P(92)49

V.P. Bhatnagar, J. Jacquinot, D.F.H. Start, B.J.D. Tubbing
and JET Team

High-Concentration Minority Ion-Cyclotron Resonance Heating in the JET Tokamak

High-Concentration Minority Ion-Cyclotron Resonance Heating in the JET Tokamak

V.P. Bhatnagar, J. Jacquinot, D.F.H. Start, B.J.D. Tubbing
and JET Team*

JET-Joint Undertaking, Culham Science Centre, OX14 3DB, Abingdon, UK

** See Annex*

Preprint of Paper to be submitted for publication in
Nuclear Fusion

HIGH-CONCENTRATION MINORITY ION-CYCLOTRON RESONANCE HEATING IN THE JET TOKAMAK

V.P. Bhatnagar, J. Jacquinot, D.F.H Start, B.J.D. Tubbing

JET Joint Undertaking, Abingdon, OXON, OX14 3EA (U.K.)

ABSTRACT.

With a view to heating a 50/50 D-T reactor plasma, ion-cyclotron resonance heating (ICRH) at a power level of 10 MW has been demonstrated in the JET tokamak for minority hydrogen concentration as high as $n_H/n_{He3} \leq 1$. In high minority ICRH experiments using (H)-He3 plasmas, improved bulk-ion heating has been observed as the minority-ion tail temperature was successfully lowered to a level below the critical energy so that the tail gave more than 50% of its power to the bulk ions. At a $P_{tot}/n_{e0} \cong 2.3 \bullet 10^{-19}$ MW$\bullet$ m^3, $T_{i0} \cong T_{e0} \cong 7$keV has been obtained in limiter L-mode discharges where the global energy confinement is similar to that found in other ICRH L-mode discharges. Here, P_{tot} is the total input power, n_{e0}, T_{e0} and T_{i0} refer to the central electron density, electron and ion temperatures respectively. Also, it is shown that the results of observed tail temperature, fast-ion energy and minority density are well understood in terms of minority ICRH physics and the Stix theory. Further, it has been shown theoretically that when the wave is launched by an antenna in (0, π)-phasing from the low-field side in large and hot reactor-like plasmas, strong single-pass damping can be maintained at minority concentrations approaching that of majority and the occurence of ion-ion hybrid mode conversion-cutoff layers would be of no consequence as most of the wave power is absorbed before it reaches this region.

1. INTRODUCTION.

In the active phase of JET, and to ease ignition in a reactor, it has been proposed to use ICRH with high concentration D-minority heating in a tritium plasma [1]. Our aim is two fold: (i) to heat a D-T plasma with an ion-mixture close to 50/50 and (ii) to reduce the minority tail energy to a level below the critical energy [2] so that it preferentially heats the background ions. Both of these aims can be fulfilled simultaneously by ICRF heating of the plasma at a higher D-minority concentration since the tail temperature decreases as the minority concentration increases for a given set of parameters. At low minority concentrations, minority tail temperatures up to an MeV have been found to occur which relax on electrons and thus lead to electron heating [3]. In a reactor, from beam penetration considerations, neutral beam injection (NBI) heating is planned at MeV range of energies which again would lead to electron heating. However, transport calculations show that the most

power-efficient route to ignition in a reactor will be via the heating of ions [4]. Moreover, the response to burn control of a reactor would be faster when the plasma is heated via the ions rather than through electrons [5]. Calculations for NET/ITER show that in the minority heating, even for n_D/n_T = 30%, at least 50% of the power will go to ions [4]. As it will become apparent, ICRF heating is the one best suited for ion heating in a reactor.

In order to discuss the heating of background species by a minority ion tail more precisely, we refer to the Stix [6] paper from which the parametric dependence of the tail temperature can be described roughly as follows:

$$T_{tail} \sim \frac{M_{mino}}{Z^2_{mino}} \cdot \frac{1}{n_{mino}} \cdot \frac{<P>}{n_e} \cdot T_e^{3/2} \qquad (1)$$

where M_{mino},Z_{mino} and n_{mino} refer to the mass, charge and density of the minority species, $<P>$ is the flux surface averaged power density of the minority, n_e is the electron density and T_e is the electron temperature. From this formula, we note that minority-ion tail can be reduced by (1) choosing a minority ion whose charge and mass are such that M/Z^2 is smaller (e.g. helium-3), (2) operating at higher minority ion density, (3) using higher target electron density so that $<P>/ n_e$ is smaller and possibly a combination of the above three. However, as mentioned above, significant ion heating will occur when the tail energy is close to or lower than the critical energy which itself depends on the minority ion species mass and electron temperature. A fast ion moving through a plasma gives equal power to electrons and background ions by collisions when its energy is equal to the critical energy [2] given by

$$E_c = 16 \cdot kT_e \cdot A_t \cdot \left[\frac{1}{n_e} \cdot \sum_j \frac{n_j Z_j^2}{A_j} \right]^{2/3} \qquad (2)$$

where A_t is the atomic mass of the test ion and j is the field ion species in the plasma. For example, He3 enjoys three times higher critical energy (due to its higher mass) than H for the same background plasma and electron temperature. From the above remarks, it is clear that dominant ion heating based on tail energy and critical energy considerations can be achieved in several ways. The scheme using He3 minority [7,8] may appear to be the best but, this may not be suitable in the (D)-T phase where additional He3 will have to be introduced and will contribute to the fuel dilution. Moreover, this scheme has a drawback of being a weak damping scenario that can not tolerate high minority concentration (see below). In Table 1, we compare several (minority)-majority species scenarios where minority ion M/Z^2, E_c/T_e and E_+/E_- (for illustration, estimated from cold-plasm theory [6]) are given. Here, E_+/E_- represents the ratio of the polarization of the left-hand (in the sense of the ions) to the right-hand rotating electric field which is a rough measure of the wave damping that depends on $|E_+^2|$. Note that (H)-D is the strongest and (He3)-D is the weakest damping scenario. However, here we use the (H)-He3 scenario. Parentheses around the symbol represent the minority species. We will show in the next section that

heating at high concentration is possible in this scenario as strong wave damping is maintained even at very high minority concentrations.

In this paper, we present results of heating and confinement in the above minority heating scenario (H-minority in He3 plasmas) when operating from medium to high minority concentrations ($n_H/n_{He3} \leq 1$) to demonstrate that one can indeed operate at high minority concentrations with improved ion heating and lower electron heating ($T_{i0} \cong T_{e0}$) at a given P_{tot}/n_{e0} while maintaining the usual confinement properties of ICRF heated discharges. It will also be shown that these results are well understood in terms of the minority ICRH physics [6,9 – 11].

The paper is organised as follows. In Section 2, we briefly review and discuss the physics basis of minority heating to show that (H)-He3 scenario is the one best suited for high-minority concentration ICRH experiments. In Section 3, we present experimental results of heating and confinement obtained in this scheme. Also, we compare these results to other ICRH L-mode data base which was obtained at lower minority concentration ($\cong$ 5%) in (H)-D scenario. Results of the minority-ion tail temperature, as measured by a neutral-particle analyser (NPA), and its variation with the minority concentration are also shown which are compared with theoretical predictions. We also present a comparison of the stored energy in the fast ions as measured experimentally to that estimated from Stix [6] model. Also, a consistency check on the estimated minority ion concentration by the 'density-rise method' (see below) and that deduced by the fast-ion energy and the minority tail temperature is presented. Using the results given in Sections 2 and 3, we present in Section 4 an ICRH high minority concentration operating diagram for the D-T phase of JET and that of a reactor with ITER-like parameters. The discussion and conclusions of this study are contained in Section 4.

2. ICRH PHYSICS BASIS.

2.1 General Remarks: For the propagation of fast magnetosonic waves, excited by an antenna carrying RF energy to the centre of a tokamak plasma composed of a minority and a majority species, an additional resonance the so called, ion-ion hybrid resonance appears in the device. The mere presence of this resonance increases the local E_+ component of the wave electric field. The damping of the wave (or the power absorbed by ions) increases as $|E_+^2|$. If the minority concentration is sufficiently low, the hybrid resonance can overlap the minority ion cyclotron resonance layer (which is Doppler broadened due to a given $k_{//}$ and $v_{//}$ in a magnetic field of the tokamak varying as 1/R) and can lead to a strong damping. Here, $v_{//}$ is the parallel velocity of the minority ions and R is the major radial position of the tokamak. A warm plasma dispersion diagram of such a scenario together with E_+/E_- is illustrated in Fig. 1 for two minority concentrations. For parameters see the figure caption. In this diagram, the two characteristic fast and ion-Bernstein waves have been identified and the location of the minority cyclotron position has been marked. Note that when $n_H/n_D = 0.05$, the fast wave perpendicular propagation constant ($k_\perp^2$) has a small wiggle near the the ion-ion hybrid resonance and close to which E_+ also rises. When the minority ion concentration is increased (to say $n_H/n_D = 0.3$), keeping other

parameters fixed, the fast wave encounters a non propagating region or a gap. It encounters a cutoff ($k_\perp^2$ goes through zero) on the low-field side of the gap whereas it is mode converted to the ion-Bernstein wave on the high-field side of the gap. Both the hybrid resonance (which is close to the mode conversion region) and the cutoff move further away from the cyclotron layer as the minority concentration is increased [12,13]. Note that now the E_+ is smaller over the cyclotron layer width though it goes to a maximum at the cut-off [10]. This reduces the minority cyclotron damping. See Table 1, for a comparison of the distance between the cyclotron layer and the cutoff (Δ_{cc}) for $n_{mino}/n_{maj} = 0.1$ in several practical scenarios [13].

Let us first point out the behaviour if the wave were to be launched from the high-field side. As the minority concentration increases, the minority damping decreases and with the appearance of the cut off and the non propagating region, the wave starts to mode convert and partially tunnel through. Further increases in minority concentration reduce tunneling and practically the entire wave power is mode converted leading generally to electron heating (see also Ref. 14) and no eigen modes are expected. In this case, the occurence of mode conversion is a fairly good indication of the change of behaviour from minority heating to mode conversion heating .

Now, if the wave is launched from the low-field side (as in most of the present-day tokamaks), at the first appearance of the gap region, a part of the energy can be mode converted to the Bernstein wave via tunneling through the cutoff confluence gap (Δ_{cm}) and a part transmitted and a part reflected. A further increase in the minority concentration increases both Δ_{cc} (see Fig. 1) and Δ_{cm} [12,13] even more. The cyclotron damping and the tunneling (transmission and mode conversion) are greatly reduced. This situation leads to the occurence of radial eigenmodes by reflection of the fast wave between this cutoff and the one located at the plasma edge near the antenna [6,15,16]. With the low-field side launch, strong single pass absorption and minority heating are the more important considerations which, in small devices, are effected signficantly as the cutoff and mode conversion appear. But in a reactor, as we will show below, the appearance of the mode conversion would be of no consequence since the wave would be significantly damped in traversing the cyclotron layer before it arrives at the cutoff-confluence region as the damping per pass will be stronger.

2.2 Mode Conversion Condition: Let us first look at the mode conversion condition and compare its behaviour in several scenarios. This will give us a first insight as to the behaviour that we may expect when more important wave damping calculations are made in the next section. The occurence of mode conversion can be identified by examining the dispersion relation of the fast wave. The condition for mode conversion can be written simply as [10,12,13].

$$\varepsilon_{xx} - n_\parallel^2 = 0 \qquad (3)$$

where ε_{xx} is th xx-component of the dielectric tensor and $n_\parallel$ is the parallel refractive index. The mode conversion can be avoided if the following condition is satisfied:

$$\left(\frac{n_{mino}}{n_{maj}}\right)_{crit} \lesssim 2 \bullet \frac{k_{\parallel} v_{\parallel}}{\omega}\left[\frac{Z_{maj}^2 M_{mino}}{Z_{mino}^2 M_{maj}}\right]\left\{\frac{1}{1-\left(\frac{Z_{maj}/M_{maj}}{Z_{mino}/M_{mino}}\right)^2}+\frac{k_{\parallel}^2 c^2}{\omega_{pmaj}^2}\right\} \quad (4)$$

where $v_{\parallel}$ is the velocity obtained from the minority ion parallel temperature and other symbols have their usual meaning. For typical JET parameters, the last term may be neglected. From Eq. (4), we note that to remain in the minority heating regime whilst using higher minority concentration (to lower the tail and heat the background ions), we should operate at higher $k_{\parallel}$ or (0, π)-phasing, use higher $v_{\parallel}$ and select appropriate (minority)-majority species. In Fig. 2, n_{min}/n_{maj} as a function of $v_{\parallel}$ normalized to the parallel phase velocity of the wave is plotted for several combinations of (minority)-majority species scenarios that can be used in JET. Electron density used for all scenarios was $5 \bullet 10^{19} m^{-3}$. The toroidal field and the frequency for each case was chosen such as to locate the minority cyclotron layer near the center of the device. As can be seen, (H)-He3 plasma offers the best combination for minority heating at higher minority concentration. Note that Eq. (4) is plotted in Fig. 2, as a universal plot, in the simplest x-axis ($v_{//mino}/v_{//ph}$) dictated by Eq. (4) so that the effect of Z/M of minority-to-majority species of different scenarios is explicitly brought out. However, this choice is by no means unique and other ways of plotting the same equation are possible and have been done such as, for example, plotting n_{mino}/n_{maj} against minority ion β (kinetic to magnetic pressure), or minority average energy (see below) etc. We must point out that when comparing different (minority)-majority species scenarios, the effect of mass on $v_{//mino}$ and frequency of operation (on v_{ph}) should be kept in mind. Also, the effect of ion charge (such as for He3) will influence the value of $(n_{mino}/n_{maj})_{crit}$ which is raised when He3 is majority and lowered when He3 is minority species. The shaded regions in Fig. 2 indicate roughly the operating domains in JET for minority heating when operation at strong single pass absorption (SPA > 0.8) is carried out. Operation at higher minority concentration than these is accompanied by a decreasing SPA (see below). We point out that the shaded regions extend roughly vertically down when operation at lower minority concentration is carried out. More informative operating diagrams are presented in the next section.

In Fig. 3, we show fast-wave roots in a dispersion diagram in which $k_{\perp}^2$ is plotted as a function of X ($\equiv R - R_0$) along the tokamak midplane for (H)-D and (H)-He3 plasmas with $n_H/n_D = 0.3$ and $n_H/n_{He3} = 0.75$. For parametres see the figure caption. Here R_0 is the tokamak major radius. The plot shows that indeed there is no cutoff and no mode conversion even for $n_H/n_{He3} = 0.75$ as compared to the case shown for (H)-D plasma, where the cutoff has already occurred at $n_H/n_D = 0.3$.

Using the ray tracing code BRAYCO [17], in Fig. 4, we present the fast-wave single pass absorption as a function of n_H/n_{He3} for two isotropic minority tail temperatures and two $k_{//} = 3$ and 7 m^{-1} for JET plasma parameters as given in the figure. Here, $k_{//} = 3$ and 7 m^{-1} represent typical values of the excited spectrum in the monopole (0,0) and dipole (0, π)-phasing of the JET A1-antennas (see section 3.2). We note that practically full single pass absorbtion (SPA) can be obtained when the antenna is used in the dipole phasing whereas for the monopole phasing, the SPA

decreases in the usual fashion [18] as n_H/n_{He3} increases. We point out that though the minority temperature was not determined self-consistently, but as will be shown in Section 3.4, the values used in these calculations are representative of those found in the experiment.

For completeness, we also present in Fig. 5 a comparison of the 2-D (velocity space) minority ion distribution function after it has reached the steady state for an ICRH power density of 1 W/cm^3 in (H)-D and (H)-He3 scenarios for $n_H/n_D = 0.1$ and $n_H/n_{He3} = 0.75$. For other parameters see the figure caption. This calculation was made using a time-dependent bounce-averaged Fokker-Planck code BAFIC [19]. Here, the normalized parallel velocity is plotted against the normalized perpendicular velocity where the normalization is done by v_0 obtained from the background ion Maxwellian isotropic temperature. It is clearly seen that the perpendicular tail is much reduced at high-minority concentration with minor effect on the parallel tail which is principally affected by the pitch-angle scattering in the minority ion cyclotron heating. Consequently, the anisotropy of the distribution function is greatly reduced at higher minority concentration.

2.3 Ion-Heating Considerations As mentioned in the introduction, for significant ion heating, the minority-tail energy should be close to or below the critical energy E_c. In this section, we use the Stix [6] model of minority heating to calculate the tail temperature and plot this as a function of minority concentration for a given set of other parameters to produce an operating diagram (see also Ref. 20). The minority tail as calculated by the Stix model has been found to be in good agreement with that obtained by a more elaborate Fokker-Planck calculation (BAFIC Code) shown in the previous section. Here we restrict ourselves to (H)-He3 and (H)-D scenarios. Using the full isotropic Stix model [6], we plot n_H/n_{He3} in Fig. 6 as a function of minority tail average energy $<E>$ obtained by integration over the minority distribution function for the (H)-He3 scenario. Two curves are shown in which the ICRH power density ($<P_{ICRH}>$) was 0.5 and 1 Wcm^{-3} which is typical of JET operation. For parameters see the figure caption. These curves indicate that the equivalent perpendicular tail temperature ($T_t = 2/3 \bullet <E>_{mino}$) depends inversely on the minority concentration and that it increases with increasing RF power density. The critical energy of minority hydrogen for the parameters used is also shown. Using the data from such curves (T_t and n_H/n_{He3}) for a number of RF power densities, we produced a large mesh of points covering the whole diagram. At these points (about 600), we then calulated the single pass absorption (SPA) for $k_{//} = 7m^{-1}$ using the ray tracing code BRAYCO [17]. Contour plots of the SPA are then generated and are as shown in Fig 6. Note that the peak of the SPA hill is at about $<E> \cong 145$keV and $n_H/n_{He3} \cong 0.75$. At a given minority tail energy, as the minority concnetration is decreased, the SPA decreases slowly as shown. The SPA also decreases as the $<E>_{mino}$ is reduced at high minority concentrations. For reference, on the same graph, we plot the minority/mode conversion condition (see Eq. 4) as a function of minority average energy (where $T_{//} \equiv 1/3 \bullet <E>_{mino}$) for two values of $k_{//}$ representing the monople and dipole operation of JET A1-antennas. The region around the intersection of $k_{//} = 7m^{-1}$ with those of Stix-model curves represent roughly the operating domain in JET at about 95% of the SPA. As the minority

concentraion is decreased at a fixed electron density, the tail temperature will increase and the operating point will move along the Stix-curves for a given minority power density. One can operate at higher concentration but at lower values of SPA reaching say about 0.6 at $n_H/n_{He3} \cong 1$.

The Stix-calculation also provides the fraction of power that is being transferred to electrons and ions from the minority species. In Fig. 7, we plot the ion fraction as a function of average energy of the minority-ion tail for three cases, namely, (H)-D, (H)-He3) and (D)-T scenarios where the parameters typical of JET operation used are indicated in the inset. The value of minority concentration for each scenario, for illustration, was taken roughly from the strong SPA operating domain as indicated in Fig. 2. The curves given in Fig. 7 were produced by making the Stix calculation at several RF power densities where the minority ion distribution function, its average energy $<E>$ and the power transfer to electrons and ions are calculated simultaneously. Note that the power given to background ions decreases as the minority tail energy increases since the minority ions collide increasingly with electrons. For a single fast ion, half the power is given to ions at $E = E_c$. However, we find that at $<E> = E_c$, the fraction of power being given to ions is about 40% when full minority distribution function as well as the decrease of E_c with increasing minority concentration are taken into account. We note that in these calculations, minority ion self collisions are not taken into account. For a discussion see section 5.

Referring now to Fig. 6, we note that for $P_{ICRH} \cong 1 Wcm^{-3}$, $k_{/} = 7m^{-1}$ and $n_H/n_{He3} = 0.62$ the average tail energy is about 65 keV which is lower than the critical energy $E_c = 85$ keV. Thus such an operation would lead to a relaxation of the minority tail appreciably on the background ions. In this case, about 45% of the minority power is given to background ions leading to a significant ion heating. As we will show in section 3.4, this is in broad agreement with what we actually observe during high minority heating experiments. Also, we point out that though we use here the Stix isotropic model, it is not unrealistic at low tail energies that are relevant in the ion-heating regimes.

As a further comparison, we present a similar calculation in Fig. 8 for the (H)-D scenario where the parameters are as given in the figure caption. Note that now the peak of the SPA hill occurs at $n_H/n_D \cong 0.1$ whereas in (H)-He3 case it was at $n_H/n_{He3} \cong 0.75$. Since (H)-D is a strong damping scenario, we note that operation at say SPA = 0.6 can be achieved for $n_H/n_D \cong 0.55$ whereas in (H)-He3 for the same value of SPA = 0.6, we can operate at $n_H/n_{He3} \cong 1$. For the parameters used in the case of (H)-D the critical energy is about 100 keV. With an operation at $n_H/n_D \cong 0.35$, one could reduce the tail in this case to a level of critical energy so that about 45-50% of the tail energy could be given to the background ions (see also Ref. 19).

3. EXPERIMENTAL RESULTS.

3.1 Experimental Set-up: JET (Joint European Torus) is a D-shaped large tokamak [21] with major radius $R_0 = 2.96$ m, minor radius $a_p = 1.2$ m, nominal toroidal field $B_\phi = 3.4$ T, plasma current $I_p \leq 7$ MA, and plasma elongation = 1.6. For the results presented in this paper, $I_p = 3$ MA, $B_\phi \cong 3$ T and the ICRH frequency of operation $f = 42.6$ MHz was used. The plasma composition was a mixture of hydrogen and helium-3 gases where hydrogen concentration was varied.

In this paper, we present the data obtained in limiter plasmas additionally heated by ICRH alone. See Fig. 9 for an illustration of the plasma configuration obtained from the IDENTC equilibrium-code [22] which reconstructs the plasma flux-surfaces from the measurements made by a series of coils located close to the vacuum-vessel wall. The plasma was leaning on the belt limiters and it was well aligned to the ICRH antenna profile. The location of cyclotron layers of H and He3 are also shown.

For general tokamak diagnostic systems including that of JET see, for example, a review paper by Orlinskij and Magyar [23] and references therein. In the data presented here, the minority-ion tail temperature was measured by a mass resolved time-of-flight neutral particle analyser (NPA). See, for example, Ref. 23. The ion temperature in the central region was measured by Doppler broadening of the Ni-XXVII spectral line by a high resolution X-ray crystal spectroscopy (KX1) [25] technique. The minority-ion concentration was principally estimated by the 'density rise method' (see section 3.3).

3.2 ICRH Antenna System: The ICRH system of JET [26,27] consists of a total generator power of 32 MW, 20 s, 25-55 MHz and uses eight antennas that are distributed symmetrically around the torus. A JET antenna has two radiating elements that are separated toroidally which can be phased arbitrarily but are generally driven in (0,0)-phasing (monopole) or (0, π)-phasing (dipole). The antenna screens are made of one tier of beryllium rods [28]. In JET ICRH specific impurities have been reduced to negligible levels in all conditions of ICRH operation in JET.

3.3 Minority Concentration: There are several ways in which concentration of minority species can be determined in the plasma but most of them have large error bars. Since we would like to know the minority concentration deep in the centre of the plasma, perhaps the most reliable method could be to determine it by the CXRS-method [29] but this is not available routinely as one needs to inject a neutral beam for diagnostic purposes. Minority concentration can be determined by using a mass resolved NPA [24] by an analysis of the measured integrated flux of the species. In a large size plasma such as that of JET, this flux is somewhat weighted to the outer part of the plasma and a complex modelling of particle orbits is required to get the species concentration in the centre. Other authors [30] have used the ratio of intensities of, for example, H_α/D_α but this again relates to the density near the edge of a hot plasma. We note further that some consistency checks could be obtained by

simply determining the quantity of gas or the number of atoms of the minority and majority species injected in the device by the gas introduction system. This method can not be relied upon as the recycling and impurity release from the first wall may play a significant role. From the above discussion it is clear that an accurate determination of minority concentration in the centre is less than straightforward.

Here, we use another procedure which we term as the 'density-rise method'. It is based on the rise in the central electron density due to the minority gas puff and the minority density is evaluated using the charge neutrality condition. A practical disadvantage of this method is that a gas puff of the desired species is to be made without changing the flow of other gases in the device. This excludes density controlled feedback of gas in the chamber which is often used in tokamaks. However, for the experiments described in this paper, majority and minority species gases were puffed sequentially and therefore this method is attempted to determine the minority concentration. In Fig. 10, we show an example of time traces of the central electron density (n_{e0}), effective charge (Z_{eff}) and the RF power. The majority He3 gas feed started at about 0.5 s and was maintained constant. The hydrogen gas was additionally puffed from 4.5 s as indicated in the figure. We use the charge neutrality condition in the two time domains referred to in the figure and define the plasma effective charge as

$$Z_{eff} = \left[\frac{1}{n_e} \cdot \sum_j n_j Z_j^2 \right] \tag{5}$$

where n and Z refer to the density and charge of different species of the plasma including minority, majority and impurities. If we assume that only a single impurity ion is dominant in the plasma (such as Be or C), the minority and majority species density can be written as ($Z_i \neq Z_{mino}$ or Z_{maj}):

$$n_{mino} = \left[\frac{Z_i(n_{e02} - n_{e01}) - (n_{e02}Z_{eff2} - n_{e01}Z_{eff1})}{Z_{mino}(Z_i - Z_{mino})} \right] \tag{6}$$

and

$$n_{maj} = \left[\frac{n_{e01}(Z_i - Z_{eff1})}{Z_{maj}(Z_i - Z_{maj})} \right] \tag{7}$$

where subscripts mino, maj and i refer to the minority, majority and impurity species respectively. Subscripts 1 and 2 in n_{e0} and Z_{eff} point to time domains 1 (before) and 2 (during the minority puff) as indicated in Fig. 10. Note that this evaluation takes into account the change of Z_{eff} such as, for example, due to additional heating of the discharge. For the data shown in Fig. 10, it is estimated that the value of $n_H/n_{e02} = 0.15$ or that of $n_H/n_{He3} = 0.53$ where we have assumed the value of $Z_i = 6$. Such estimates of the minority concentrations will be used in the results presented below. The main errors on this calculation are the assumptions that a single impurity ion (C^{6+}) determines the Z_{eff} and that the density rises due to the minority species

entering the centre of the plasma without any other additional effects including that of particle transport.

3.4 Time Traces of a Low and High Concentration Minority Heating: Typical time traces of minority ICRF heating in 3 MA (H)-He3 limiter plasmas at about 10 MW of RF power are shown in Fig. 11 for two cases (a) low minority concentration ($n_H/n_{He3} \leq 0.06$) and (b) high minority concentration ($n_H/n_{He3} \leq 0.63$). In case (b), the minority concentration was measured as described above. The discharge shown in Fig. 11 (a) was taken from an earlier series in which no additional minority hydrogen was being puffed in and the residual hydrogen in the tokamak walls was contributing to the minority concentration. The plasma stored energy measured by a diamagnetic loop (W_{DIA}) is shown. The level of $W = W_G$ is also shown where W_G is the Goldston L-mode prediction [31]. It is seen that in case (a) with low minority concentration $T_{e0} \cong 8.5$keV and $T_{i0} \cong 5.5$keV whereas in case (b) with high minority concnetration $T_{e0} = T_{i0} \cong 7$keV. The equipartition power between electrons and ions in such discharges was less than 10%. By operating at a higher minority concentration, we have increased the ion temperature but decreased the electron temperature. As will be shown in the next section, at higher minority concentration the minority tail is shorter and gives more power to ions (see Section 2.3). The total radiated power P_{RAD} from the plasma as measured by an array of bolometers shows that in case (b) $P_{RAD}/P_{TOT} \cong 0.25 - 0.3$ and it is slightly higher in case (a).

3.5 Minority Distribution Function Measurement: The H-minority perpendicular ion energy distribution function as measured by a mass resolved neutral particle analyser (NPA) is shown in Fig. 12 for several time slices as indicated in the inset where the RF power waveform is also shown. The tail temperature (T_t) during the RF flat top is about 50 keV. Note that $T_t \cong 20$keV even 0.5 s after the RF is switched off which is significantly above the ohmic value. The minority tail near E_c would relax on the background species with a slowing-down time of about 0.3 s which appears to be somewhat faster than observed. The theoretical minority distribution function for the time slice 3 from the isotropic Stix model is also shown for comparison. For simplicity, we use isotropic model as the tail energies are near the critical energy. The tail temperature obtained from the higher energy part is roughly the same but at lower energy there is a significant difference between the perpendicular (measured) and isotropic (theory) distribution function due to the difference in pitch-angle scattering. The T_t measured using the NPA diagnostic for several such discharges is plotted in Fig. 13 as a function of n_H/n_e where the minority concentration is determined using the density-rise method. Fitted to a central point, the broken line drawn represents the expected $[n_H/n_e]^{-1}$ dependence of the tail temperature such as also found in Fig. 6. The error bars on n_H/n_e deduced from the density rise method have been discussed in Section 3.3. The vertical error-bar reflects the error on the NPA and the drawing of a straight-line through the data points to deduce a T_t. Thc numbers on the top x-axis give approximate values of n_H/n_{He3} for a corresponding n_H/n_e.

In these discharges, the critical energy was roughly about 75 keV. We therefore note that we have succeeded in lowering the tail temperature close to or below the critical energy at 10 MW power level resulting in improved ion heating such that $T_{i0} \cong T_{e0}$. Operation at low minority concentration leads to stronger tails and $T_{e0} > T_{i0}$ (see Section 3.6).

3.6 Ion and Electron Heating: The central bulk-ion temperature (T_{i0}) as measured by the KX1 (see section 3.1) diagnostic for a series 3 MA discharges with high minority concentration in (H)-He3 plasmas is plotted (solid squares) in Fig. 14 as a function of P_{TOT}/n_{e0} where P_{TOT} is the total input power and n_{e0} is the central electron density. For comparison purposes we have also plotted (open circles) the T_{i0} data obtained in 3 MA ICRH limiter discharges [32] in low minority concentration ($n_H/n_D \cong 5\%$) in (H)-D plasmas. At a given $P_{TOT}/n_{e0} \cong 2.3 \cdot 10^{-19}$ MW $\cdot$ m^3, it is found that T_{i0} is higher by about 15-20% when compared with (H)-D discharges at lower minority concentration. See section 5 for a discussion of obtaining higher T_{i0} in other ICRH scenarios. A similar plot of T_{e0} is shown in Fig. 15 for discharges with higher minority concentration and compared with low minority discharges as in Fig. 14. A comparison of solid squares and open circles show that T_{e0} in the high minority heating is similarly lower by about 10-20%. For a discussion of NBI data points, see Section 5.

3.7 Energy Confinement: A plot of stored energy W (from diamagnetic loop measurement) plotted as a function of loss power (P_{TOT}-dW/dt) for a series of high minority heating discharges at $I_P = 3$ MA is shown in Fig. 16. The three broken lines represent the Goldston [31] L-mode prediction W_G, $1.5W_G$ and $2W_G$ respectively, for such high-minority concentraion (H)-He3 discharges where an average mass of the ion mixture has been taken into account. We note that $\tau_E \cong 1.25\tau_G$ as found in other ICRH L-mode discharges [32] at 3 MA obtained at lower minority concentration heating of (H)-D plasmas. The stored energy data in which the fast-ion energy (see Section 3.4) has been subtracted is also plotted for reference.

3.8 Fast Ion Energy (Comparison of Theory and Experiment): Fast ions produced during the minority ICRH are well confined in JET for discharges at a plasma current of 3 MA presented in this paper. These fast ions contribute to the total stored energy of the plasma. Using the Stix model [6] we can calculate the average energy of the minority species locally using the ICRH power deposition profiles obtained from, for example, ray-tracing calculations [17]. For simplicity, we make an assumption that ICRH power is deposited uniformly in a radius of 0.45m (volume of 17.6 m^3) which is based on a Doppler width with a $T_t \cong 50$keV (see Fig. 13) and $k_{//} = 7\text{m}^{-1}$ (dipole), and taking account of slightly off-axis location of the cyclotron layer in these discharges. This allows us to estimate the average ICRH power density to calculate theoretically the Stix minority-ion distribution function such as that shown in Fig. 12. This calculation also provides the minority-ion average energy. Using the minority density deduced from the density rise method (see Section 3.3), we calculate the energy stored in the minority ions.

Fast ion energy in these experiments has also been determined by measuring the diamagnetic stored energy (W_{DIA}) and that obtained by equilbrium reconstruction (W_{MHD}) using the relation $W_f \equiv 1.33 \bullet (W_{DIA} - W_{MHD})$ [33]. In principle, this procedure gives a measure of the anisotropic part of the fast-ion energy. To compute a similar quantity theoretically, one has to calculate the perpendicular as well as the parallel minority ion distribution functions which could be done, for example, using the bounce averaged 2-D Fokker-Planck code (BAFIC). Alternatively, anisotropic Stix model could be used for the perpendicular energy but the parallel energy is not properly calculated and is only estimated. However, the high-energy tail temperature obtained by the anisotropic Stix-model agrees well [34] with the one calculated by isotropic Stix-model although the detail of the distribution function differ slightly at low energies due to pitch-angle scattering. Therefore, the average energy of the minority distribution function obtained from the isotropic model is a fair representation of the anisotropic part when we subtract out the low-energy Maxwellian part of the distribution function. The socalled 'theoretical' values of the minority fast ion energy calculated in this way are compared in Fig. 17 to the experimental values mentioned above. The agreement between the two quantities is fair considering the error bars on the measurements (W_f is the difference of two measured quantities) and calculations (assumption of uniform power deposition, errors on minority-density evaluation and a neglect of parallel energy of the fast ions).

We now go a step further to make a consistency check on our measurements of the minority concentration by determining the minority density from the experimental measurement of stored energy W_f (see above) in the fast ions and the minority tail temperature measured by the NPA diagnostic. Again making the assumption that ICRH power is deposited uniformly, the minority density can be deduced from the relation

$$\frac{n_{min}}{n_{e0}} \cong \frac{W_f(MJ)}{28 \bullet T_t(MeV) \bullet n_{e0}(10^{19}m^{-3})} \tag{8}$$

A plot of n_H/n_{e0} obtained from this procedure is plotted in Fig. 18 against the minority concentration obtained from the density rise method (see section 3.3). Ideally the points should lie along the 45°-line. The agreement is fairly good.

4. OPERATING DOMAIN OF FUTURE EXPERIMENTS.

4.1 (D)-T Phase of JET: Using the same procedure as discussed in Section 2.3, we now present a possible operating domain for the ICRF heating of a high concentration (D)-minority in a tritium plasma. Figure 19 shows a plot of n_D/n_T vs average energy of the D-minority ions for two values of minority-ion power densities using Stix theory. For the parameters that are as given in the figure caption, the critical energy E_c of deuterium is also shown. Further, we show single pass absorption (SPA) contours in this case. On the same graph, we plot the minority/mode conversion condition (see Eq. 4) for $k_{\parallel} = 7m^{-1}$ which would roughly be representative of the $(0, \pi)$-phasing of the A2-antennas that will be used in the D-T phase of JET. In this case the peak of the SPA hill occurs at $n_D/n_T \cong 0.4$. In the

(D)-T phase of JET, one could operate upto a concentration $n_D/n_T \cong 0.4 - 0.6$ for $P_d = 0.5 - 1 W/cc$ allowing a single pass absorption say a SPA = 0.6. For ICRH (D)-T operation in JET, a range of minority concentration ($0.1 \leq n_D/n_T \leq 0.6$) can be used and the the operating domain will follow the Stix curves. Since the minority tail temperatures will be below the critical energy E_c, we expect that 50-60% of the minority power will be given to background ions resulting in significant ion heating.

4.2 ICRH Operating Domain of a Reactor: We now present a similar calculation, to that shown in the previous section, for a reactor with the parameters of a ITER-like machine. The variation of minority $< E >$ as a function of n_D/n_T at two values of P_d, the mode conversion condition for a $k_\parallel = 4m^{-1}$ and the contours of single pass absorption (SPA) are shown in Fig. 20 for the parameters as given in the figure caption. In this calculation damping on the α-particles (He4) is not included which would further increase SPA but at the expense of some reduced ion heating. First we note that for these parameters, the peak of the SPA hill occurs at $n_D/n_T \cong 0.2$. The operation will follow the power density (P_d)-curves from which we note that we can operate up to $n_D/n_T \cong 0.95$ for say SPA = 0.6. From the experience in JET while operating in (He3)-D, a weak damping scenario, SPA = 0.3 would still be tolerable. Operation at such a level of SPA in a reactor would allow us to operate in a deuterium rich mixture of a D-T plasma for $n_D/n_T \leq 1.2$ but at the expense of reduced direct ion heating. A possible scenario for achieving this will be to apply roughly a square wave ICRH pulse with deuterium concentration rising to its maximum value in about 5 s. According to this diagram, the operation will follow the P_d-curves from low to high concentration reducing the tail energy and increasingly giving power to the background ions. The concentration of deuterium will be allowed to reach at its maximum to be $n_D/n_T = 1.2$, a deuterium rich mixture which is advantageous for reducing tritium inventory.

5. DISCUSSION AND CONCLUSIONS.

In the high concentration minority ion heating expriments in (H)-He3 plasma presented in this paper, we did not observe clear eigen modes on the antenna coupling resistance even at the highest minority concentration ($n_H/n_{He3} = 1$) used. According to theoretical calculations presented in Section 2.3 (see Fig. 6), single pass aborption in such conditions would be $\cong 0.5$ for antenna in the dipole phasing which is large enough to avoid eigenmodes. Eigenmodes are excited more commonly in monopole phasing as a significant part of the power lies near $k_\parallel = 0$ which is very weakly damped. The monopole phasing was not used in the high minority ($0.3 < n_H/n_{He3} < 1$) discharges.

We must point out that in the theoretical results presented in this paper using the Stix model, we have not included the effect of self collisions of the resonant minority species. This effect may be important at high minority concentration where self-collisions are expected to reduce the minority tail temperature and the power transfer to the background species. For an estimate, we made a Stix-type calculation in which minority species was used as an additional background species with an

unheated initial Maxwellian distribution to model the self collisions. In such a case the minority average energy was lower by less than 1% for $n_H/n_{He3} \leq 0.2$ as compared to that presented without self collisions. This difference was about 15% at $n_H/n_{He3} = 0.5$ and finally increasing to 25% at $n_H/n_{He3} = 1$. The effect of including the heated species more correctly by iteration, as was done in Ref. 35, is found to show little additional difference.

As mentioned in the introduction, lower minority tail temperatures to enhance bulk-ion heating can also be achieved by using two minorities (H and He3) in D-plasmas and coupling half the power in each species at two appropriate but different frequencies [36]. We reiterate that He3-minority in D plasmas, is a weak damping scenario that can not tolerate high minority concentration in JET (see Section 2.2). He3-minority would have been especially suitable for ion heating due to its charge and mass as it produces shorter tails and its critical energy is 3 times higher than hydrogen (see Table 1). In the two minority scheme also, when the experiment was carried out in the L-mode, $T_{i0} \cong T_{e0}$ is obtained just as in the high minority heating experiments presented in this paper.

For comparison, we have plotted the values T_{i0} and T_{e0} as a function of P_{tot}/n_{e0} for two neutral-beam injection (NBI) heated discharges in JET (see Fig. 14 and 15). In these limiter L-mode discharges, $(He3)^0$ beams were injected in He3 plasmas at a power level of 12 MW. We note that in comaprison to the other ICRH L-mode data, T_{i0} is somewhat higher but T_{e0} is lower. Calculations show that in the NBI case about 70% of the beam power deposited in the central region goes to ions and 30% to electrons whereas in the ICRH cases at high concentration ($n_H/n_{He3} \cong 0.55$), ICRH power is split roughly equally.

To increase the T_{i0} much beyond the T_{e0}, a combination of central ion heating and improved central ion energy confinement is required. Such a situation has successfully been achieved in the so called 'hot-ion H-mode' where the NBI power is deposited centrally in a relatively low edge-density plasma [37] that has made a transition from the L to H-mode of confinement. However, in a reactor, one would like to operate at a high-edge density from the divertor loading considerations. Stronger ion heating even at high densities can be obtained by ICRH in the peaked-density profiles or the pellet enhanced phase (PEP) [38,39]. We note that $T_{i0} \cong 16$keV ($T_{i0} > T_{e0}$) has been obtained [40] in a high density plasma $n_{e0} = 7 \cdot 10^{19} m^{-3}$ by two minority ICRF heating in PEP + H-mode experiments though the PEP-phase lasts only transiently. In such discharges again more than 70% of the power goes to ions and they have lower central ion-heat diffusivity. Majority ion heating $T_{i0} \cong T_{e0} = 10$keV has also been achieved in PEP + H mode with a single minority in (H)-D plasma where $n_H/n_e \cong 15\%$ [20].

In **conclusion** , it has been shown that strong wave damping can be maintained at high minority concentration for large and hot reactor-like plasmas heated from the low-field side in the dipole phasing of the antenna. Plasma heating by ICRF using H-minority in He3-plasmas has been demonstrated at a power level of 10 MW for minority concnetrations approaching that of majority species. The minority tail temperature was successfully lowered to a level below the critical energy so that the

tail gave more than 50% of its power to the bulk ions in the (H)-He3 sceanrio. At low minority concentration, generally $T_{i0} < T_{e0}$. But, here it has been shown that at high minority concentration, $T_{i0} \cong T_{e0} = 7keV$ is obtained in the limiter L-mode discharges where the global energy confinement was similar to that found in other ICRH L-mode discharges. The successful operation of ICRH at minority ion concentrations approaching that of majority and the evidence of improved ion heating gives confidence in the previously proposed [1] deuterium cyclotron heating of a 50/50 D-T plasma of a reactor. In fact, there will be a flexibility to work in a range of concentrations ($0.05 \leq n_D/n_T \leq 1.2$). Sawtooth stabilization process will be maximum at low concnetration but will lead to some penality such as in fuel dilution and thermal β available. Maximum direct ion heating will be achieved when $n_D/n_T \cong 0.3$. Finally, deuterium rich scenarios ($n_D/n_T \cong 1.1 - 1.2$) which are advantageous for tritium inventory purposes can be heated by ICRF but at the expense of a reduction of direct ion heating. Single-pass absorption will further improve when damping on the α-particles produced in a reacting plasma is included which will increase the range of D-minority concentration that can be used but in this condition the amount of direct ion heating will further drop.

ACKNOWLEDGEMENTS.

We wish to thank the ICRH plant team, the tokamak operation team and those operating the diagnostics used in the experiments reported in this paper. Valuable discussions with L. Eriksson are acknowledged and the help of J.J. Ellis in computational work is appreciated. We also thank C.D. Challis, S. Corti, H.P.L. De-Esch, C. Gowers, H. Morsi, J. O'Rourke, and D. Stork for help with these experiments.

REFERENCES.

[1] JACQUINOT J. et al, Plasma Phys and Contr Fusion, 30 (1988) 1467.
[2] STIX, T.H., Plasma Physics, 14 (1972) 367.
[3] JACQUINOT, J. et al, Plasma Phys and Contr. Fusion 33 (1991) 1657.
[4] KOCH, R. et al, 13th IAEA Conf. proceedings, Washington, Nuclear Fusion Supplement (1991) vol. 3, 605.
[5] KOCH, R. et al, Topical Conf. on RF Heating and Current Drive of Fusion Devices, Brussels, 1992, to be published in Plasma Physics and Controlled Fusion.
[6] STIX, T.H., Nuclear Fusion, 15 (1975) 737.
[7] HOSEA, J. et al, 8th IAEA Conf. Proceedings, Brussels, Nuclear Fusion Supplement, (1981) vol. 2, 95.
[8] BHATNAGAR V.P. et al, Proc. 13th EPS Conf. on Contr. Fusion and Plasma Heating, (1986), Europhysics Conf. Abstracts, Vol. 10C, Part II, 165.
[9] JACQUINOT, J. et al, Physical Rev. Lett. 39 (1977) 88.
[10] TAKAHASHI, H., J. Phys. (Paris) Colloq., C6 (1977) 171.
[11] PERKINS, F., Nuclear Fusion, 17 (1977) 1197.
[12] JACQUINOT, J., Proc. Varenna-Grenoble Symp. on Heating in Toroidal Plasmas, vol. 1 (1978) 127.

[13] ADAM, J., Plasma Phys Contr. Fusion, 29 (1987) 443.
[14] WEYNANTS, R.R. et al, Proc. 13th EPS Conf. on Contr. Fusion and Plasma Heating, (1986), Europhysics Conf. Abstracts, Vol. 10C, Part II, 33.
[15] McCARTHY, A.L. et al, Proc. 15th EPS Conf. on Contr. Fusion and Plasma Heating, (1988), Europhysics Conf. Abstracts, Vol. 12B, Part II, 717.
[16] DESCHAMP, P. et al, Plasma Phys Contr. Fusion, 33 (1991) 1109.
[17] BHATNAGAR, V.P. et al, Nuclear Fusion, 24 (1984) 955.
[18] BHATNAGAR, V.P. et al, Nuclear Fusion, 26 (1986) 61.
[19] HAMNEN H. et al, 'A Bounce-Averaged Fokker-Planck Ion Cyclotron Code (BAFIC)', Report JET-DN-T(85)23, JET Joint Undertaking, Abingdon, U.K. Also, BHATNAGAR, V.P., CORE, W.G. and ELLIS, J.J., (1991) Private Communication.
[20] START D.F.H. et al,(1991) Proc IOP Plasma Phys Conf, Colchester, UK.
[21] REBUT, P-H. et al, 12th IAEA Conf. proceedings, Nice, France, Nuclear Fusion Supplement, (1989) vol. 2, 191.
[22] LAZZARO, E. et al, (1987) Report JET-P(87)58, JET Joint Undertaking, Abingdon, UK.
[23] ORLINSKIJ, D.V. and MAGYAR G., Nuclear Fusion, 28 (1988) 611.
[24] CORTI, S et al, Proc. 18th EPS Conf. on Contr. Fusion and plasma Physics, (1991), Europhysics Conf. Abstracts, Vol. 15C, Part IV, 253.
[25] MORSI, H et al, Proc. 17th EPS Conf. on Contr. Fusion and Plasma Heating, (1990), Europhysics Conf. Abstracts, Vol. 14B, Part IV, 1608.
[26] WADE T. et al (1991) Proc. 14 Symp. Fusion Engg, San Diego, to be published.
[27] KAYE A.S. et al (1987) Fusion Technology, 2, 203.
[28] WALKER, C.I., Proc. 15th Symp. Fusion Techno, Utrecht, Holland, (1988) 444.
[29] Von HOLLERMANN, M. et al, Plasma Phys Contr Fusion, 33 (1991) 1805.
[30] MESSIAEN, A.M. et al, Plasma Phys Contr Fusion, 32 (1990) 889.
[31] GOLDSTON, R. (1984) , Plasma Phys. Controlled Fusion 26, 87.
[32] BHATNAGAR, V.P. et al, Plasma Phys and Contr Fusion, 31 (1989) 333.
[33] CHRISTIANSEN, J., Internal Note, JET Joint Undertaking, Abingdon, 1987.
[34] ERIKSSON, L. Private Communication, 1992.
[35] WOLLE, B. et al, Plasma Phys Contr Fusion, 33 (1991) 1863.
[36] BHATNAGAR V.P. et al, Proc 9th Topical Conf. on Radio Frequency Power in Plasmas, Charleston, USA (1991), AIP Conf Proceedings 244 (1992) 115.
[37] THE JET TEAM, Nuclear Fusion, 32 (1992) 187.
[38] SCHMIDT G.. et al, 12th IAEA Conf. proceedings, Nice, France, Nuclear Fusion Supplement, (1989) vol. 1, 215.
[39] BHATNAGAR V.P. et al, Plasma Phys and Contr Fusion, 31(1989)333.
[40] JACQUINOT J. et al, Bull. Amer. Physical Soc. Div. of Plasma Phys, 36 (1991) 2295, to be published in Phys Fluids B.

Table 1. A Comparison of Critical Energy, Field Polarization and Damping for Several Minority ICRH Scenarios. Δ_{cc} is the gap between confluence and cyclotron layers for $n_{mino}/n_{maj}=0.1$ and R_0 is the tokamak major radius.

Scenario	Minority Ion	M/Z^2	E_C/T_e	Δ_{cc}/R_0	E_+/E_-	Damping. (see text)
(H)-D	H	1	10	0.12	$\approx \frac{1}{3}$	'Strong'
(H)-He3	H	1	12.5	0.04	$\approx \frac{1}{5}$	'Medium'
(D)-T	D	2	15	0.07	$\approx \frac{1}{5}$	'Medium'
(He3)-D	He3	$\frac{3}{4}$	30	0.09	$\approx \frac{1}{7}$	'Weak'.

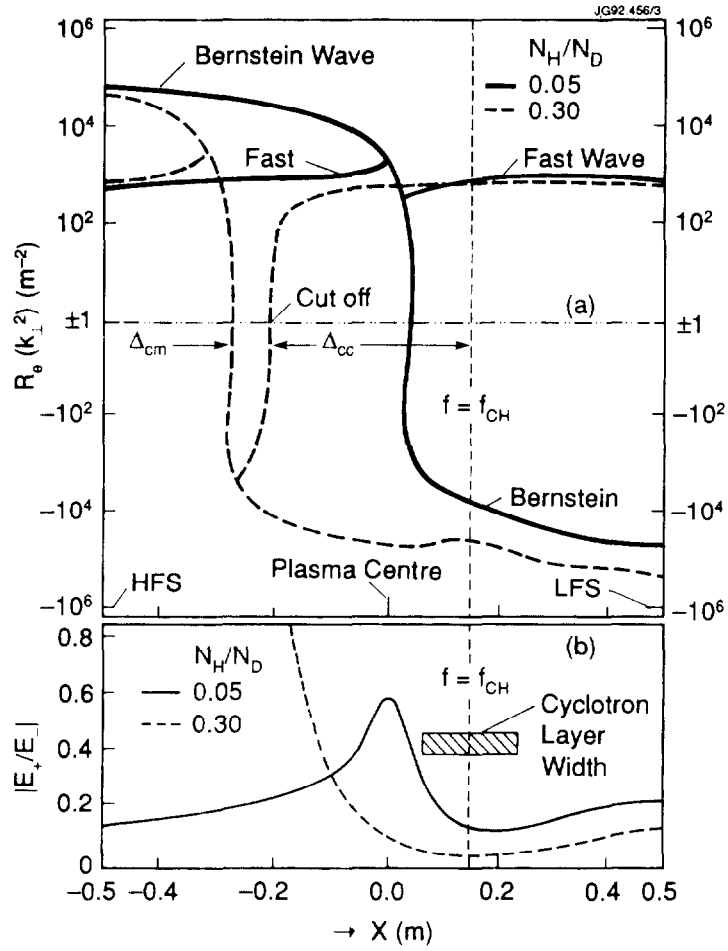

FIG. 1. (a) A plot of the real part of $k_\perp^2$ for the Fast and Bernstein waves for two values of minority concentration in (H)-D plasma as a function of $R\text{-}R_0$ in the central region of the JET tokamak. The location of the H-cyclotron layer is shown by $f = f_{CH}$. Here, Δ_{cc} is the distance between cutoff and cyclotron layer and Δ_{cm} is that between cutoff and mode conversion. Other parameters are $f = 32$ MHz, $B_\phi = 2.2$ T, $T_{e0} = 4$ keV, $T_{i0} = 3$ keV, $n_{e0} = 3 \cdot 10^{19} m^{-3}$, $k_{//} = 7 m^{-1}$. Profiles are parabolic except for density for which parabolic profile exponent $\rho = 0.6$ (b) Corresponding plot of the ratio of left-hand to right-hand polarized electric field.

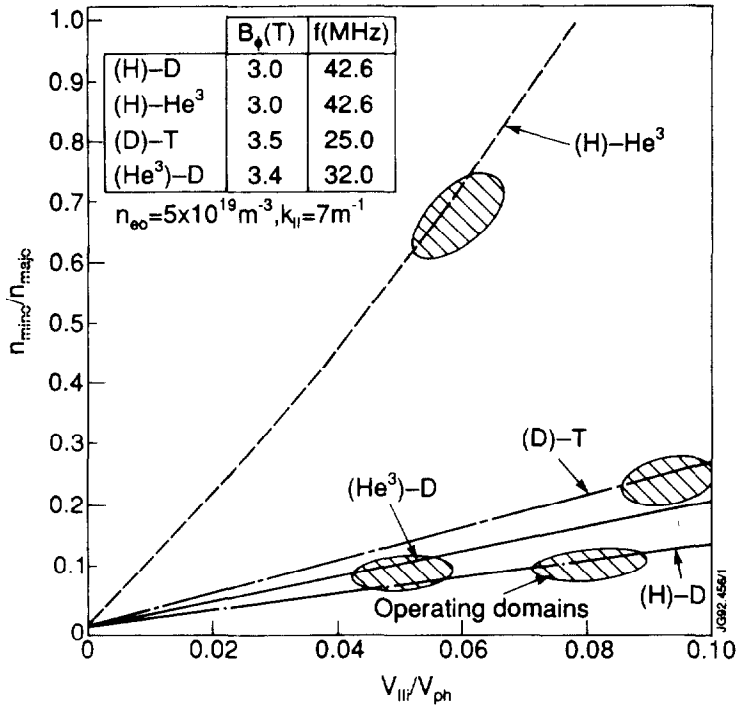

FIG. 2. Ratio of the minority-to-majority species density, above which mode conversion occurs, is plotted as a function of the ratio of minority speed $v_{//}$ (parallel to the magnetic field) to the parallel phase velocity $\omega/k_{//}$ for several ICRH minority heating scenarios. Plasma parameters are as given in the inset. Shaded regions show the typical operating domain near maximum damping of the wave (see Section 2.3).

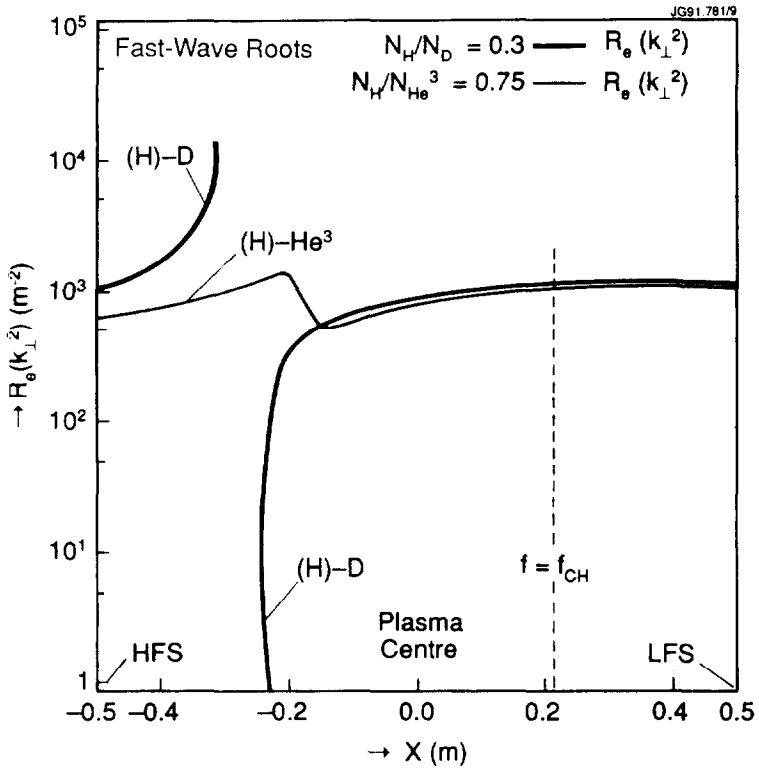

FIG. 3. A plot of the real part of $k_\perp^2$ as a function of position along the major radius in (H)-He3 and (H)-D plasmas for two concentrations of the minority. Mode conversion does not occur even at high values of $n_H/n_{He3}=0.75$. Other parameters are: $k_{//} = 7m^{-1}$, $n_{e0} = 5 \cdot 10^{19}m^{-3}$ and $T_H = 70keV$, $T_{He3} = T_D = 8keV$ and $T_e = 7keV$.

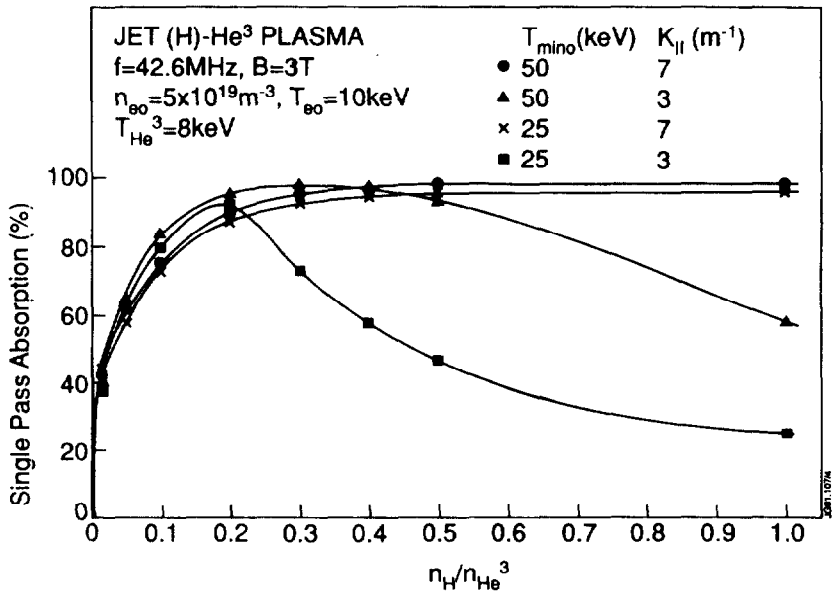

FIG. 4. A calculation of the single-pass absorption as a function of the minority concentraion n_H/n_{He3} for two values of the isotropic minority-ion temeperature and two values of $k_{||}$ typical of the (0,0) and (0,π) operation of the JET A1-antennas. Plasma parameters are as given in the inset.

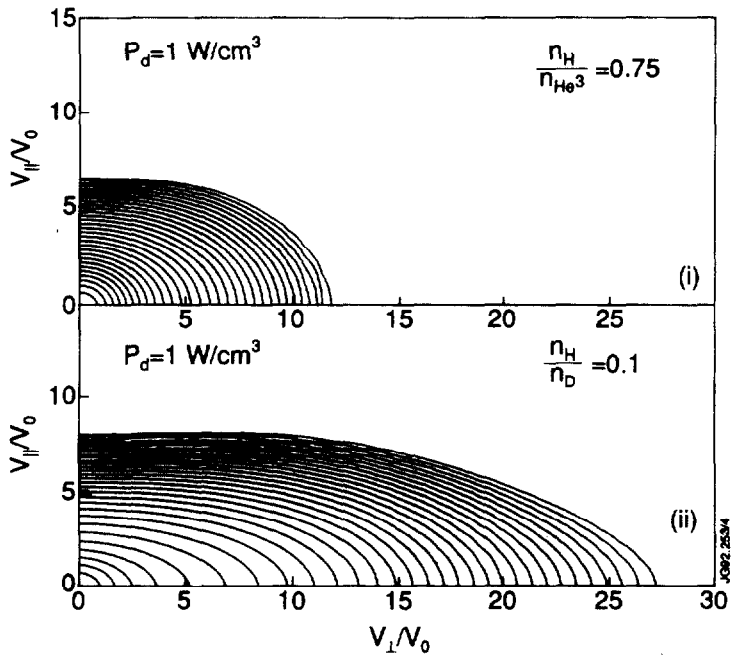

FIG. 5. The steady-state minority ion distribution function in 2-D velocity space during minority heating calculated using a time dependent bounce-averaged Fokker-Plank (BAFIC) code for two cases: (i) (H)-He3 plasma, $n_e = 5 \cdot 10^{19}m^{-3}$, T_e = 7keV, T_i = 8keV and (ii) (H)-D plasma, $n_e = 5 \cdot 10^{19}m^{-3}$, T_e = 8keV, T_i = 5keV. For illustarion, the trapping parameter has been set to zero.

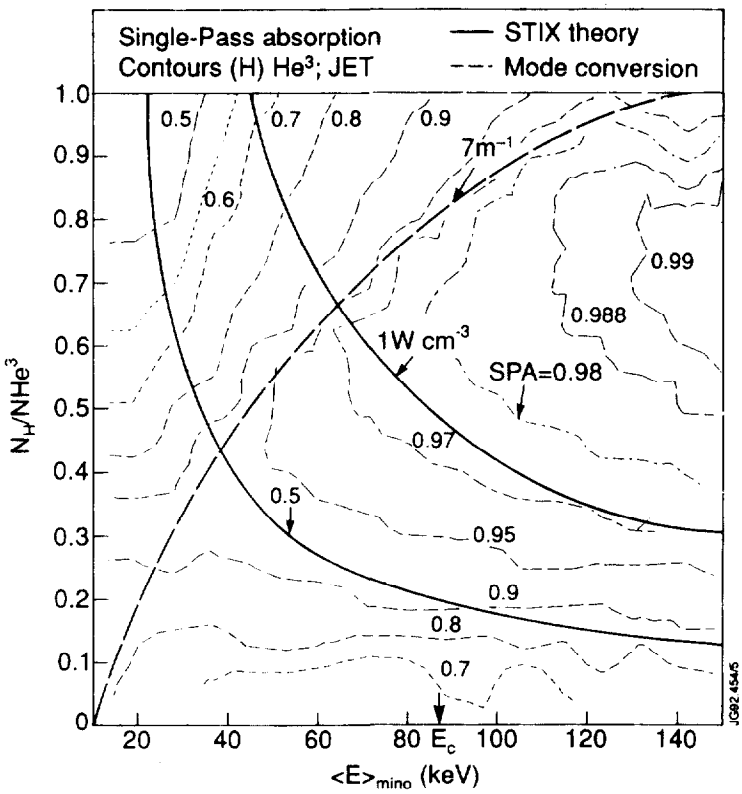

FIG. 6 A plot of n_H/n_{He3} as a function of the average tail energy of the minority based on the full Stix isotropic model for several values of the ICRH power densities in a (H)-He3 plasma. On the same diagram, single pass absorption contours are shown for $k_{//} = 7m^{-1}$. For illustration, mode conversion condition (Eq. 4) for two values of $k_{//}$ are also drawn. $T_{//} \equiv 1/3 \bullet < E >$. Also, $T_e = 7keV$, $n_{e0} = 5 \bullet 10^{19}m^{-3}$ and $T_H = T_{He3} = 8keV$.

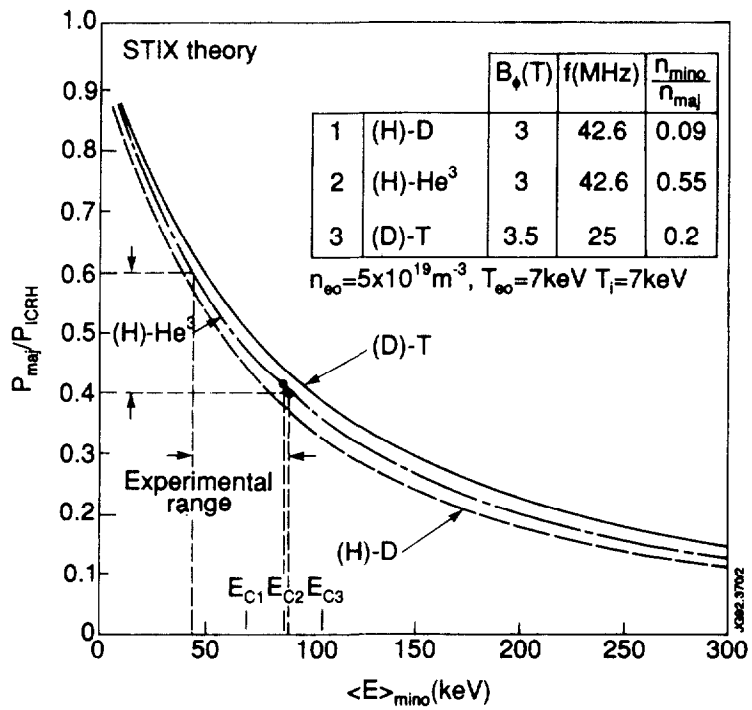

FIG. 7 Fraction of minority power given to background ions plotted as a function of the average minority energy $< E >$ for several scenarios. The $< E >$ was calculated using Stix theory for several minority power densities for the parametes indicated in the inset. Minority-ion self collisions are not included (see Section 5).

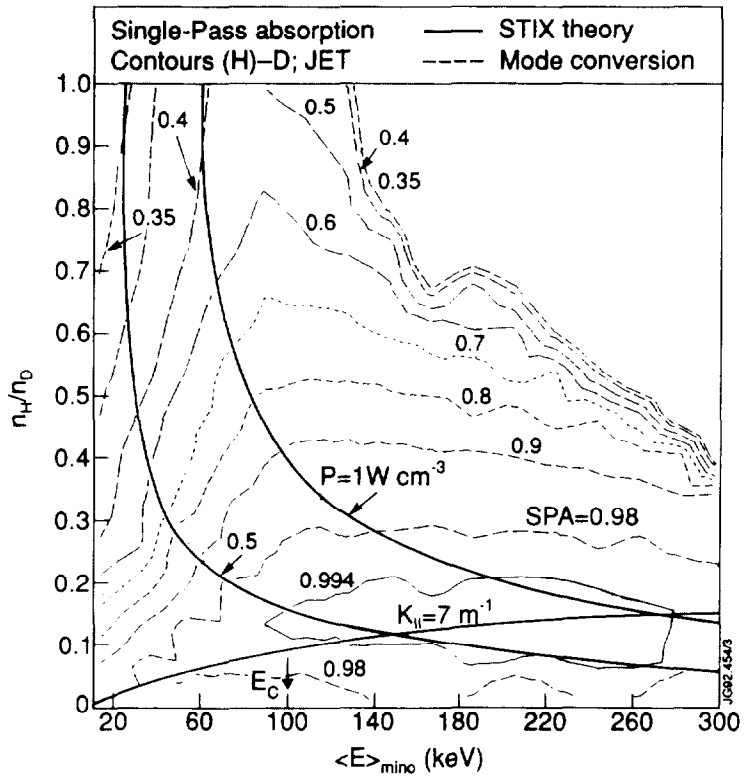

FIG. 8. Single pass absorption contours in a n_H/n_D vs minority $<E>$ diagram in a (H)-D plasma similar to Fig. 6. Other plasma parameters are: $T_e = 10$keV, $n_{e0} = 5 \cdot 10^{19}$m^{-3} and $T_H = T_D = 6$keV.

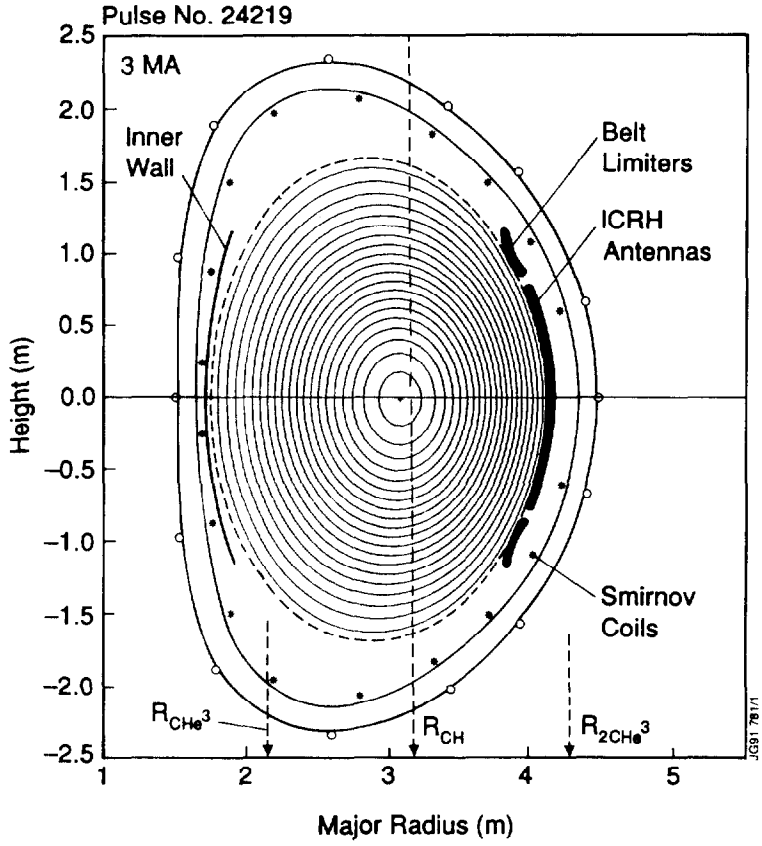

FIG. 9. Poloidal-flux contours from the IDENTC equilibrium reconstruction code showing the plasma configuration used in the present experiments. The plasma was limited by belt limiters. The cyclotron resonance positions for H and He3 are also indicated.

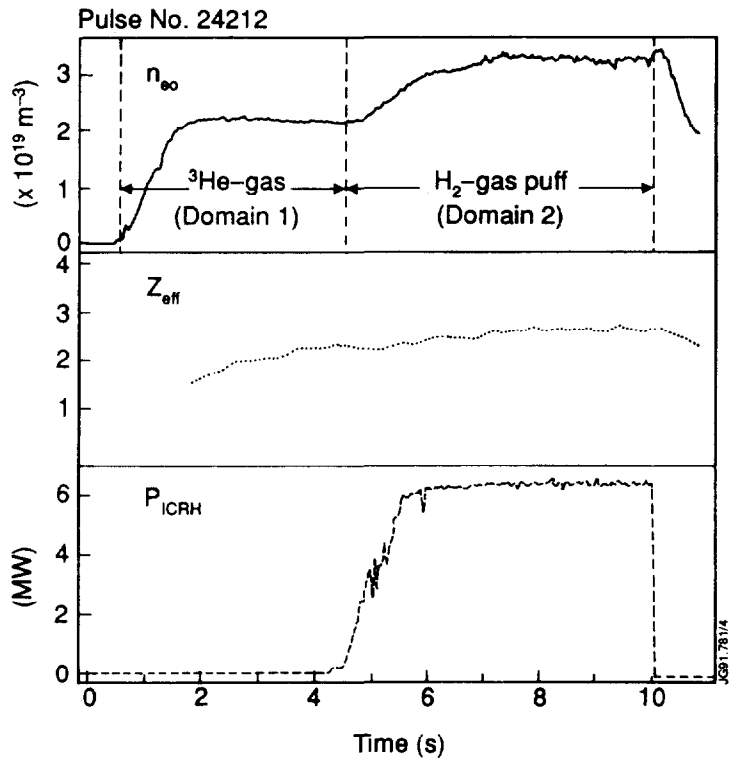

FIG. 10. Central electron density (n_{e0}), plasma effective charge (Z_{eff}) and RF power traces as a function of time. The domains 1 and 2 refer to the duration of He3-majority and H-minority gas puffs respectively. The minority ion concentration is determined by the 'density-rise method'.

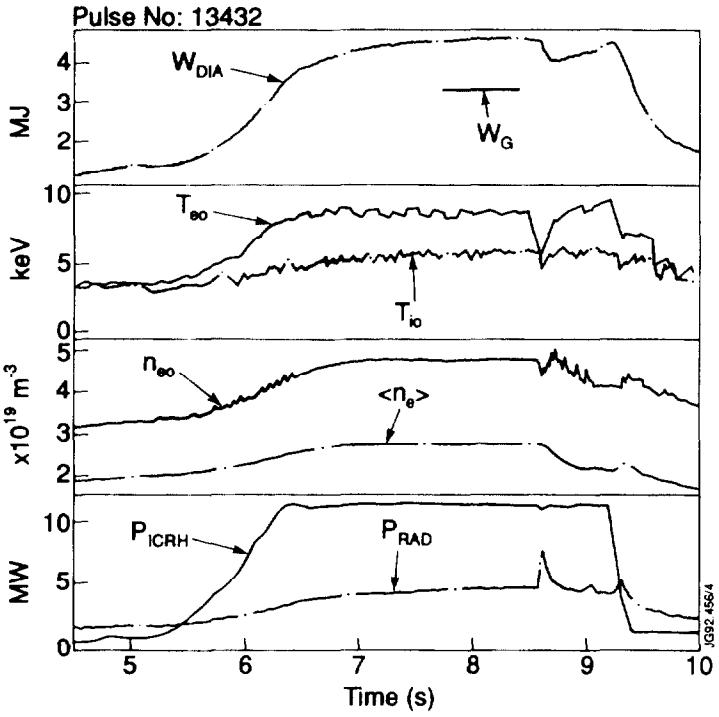

FIG. 11 (a). Time traces of a low concentration minority heating in a (H)-He3 plasma where $n_H/n_{He3} \leq 0.06$. W_G is the Goldston L-mode value. $<n_e>$ is the volume averaged density and P_{RAD} is the bolometric radiated power. See also Fig. 11 (b)

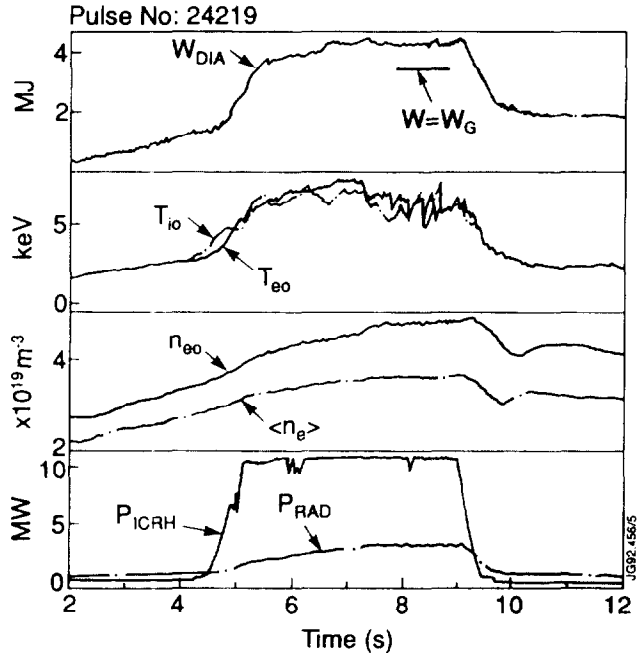

FIG. 11 (b). Time traces of a high concentration minority heating in a (H)-He3 plasma where $n_H/n_{He3} \cong 0.63$. bolometric radiated power. See also Fig. 11 (a).

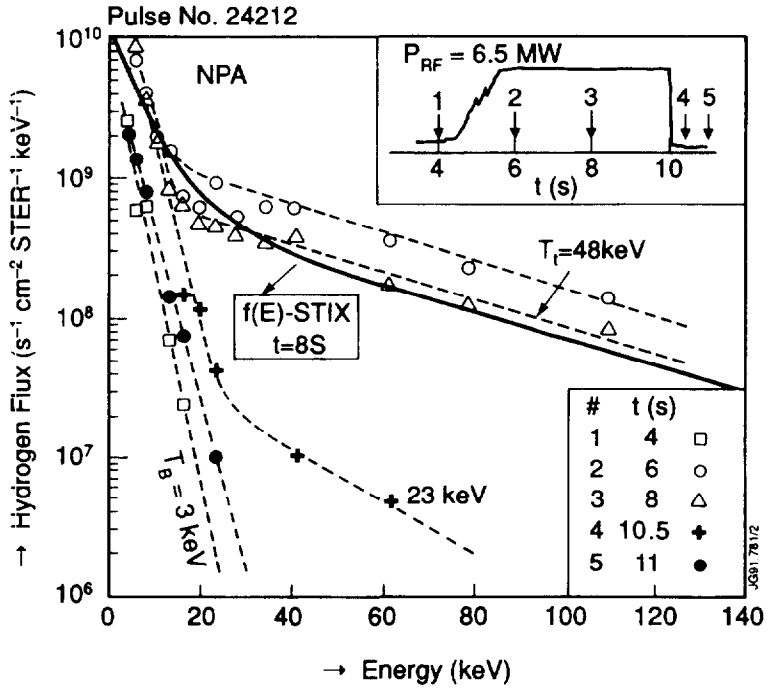

FIG. 12. A semi-log plot of hydrogen flux as a function of the particle energy measured by a NPA viewing along a vertical chord through the centre of the discharge during the high minority heating experiments ($n_H/n_{He3} \cong 0.53$). The inset shows the ICRH power trace and the arrows indicate the time slices during the RF pulse at which the data is plotted. The solid line shows the isotropic Stix distribution (theory) for the 3rd time slice. Minority-ion self collisions are not included (see Section 5).

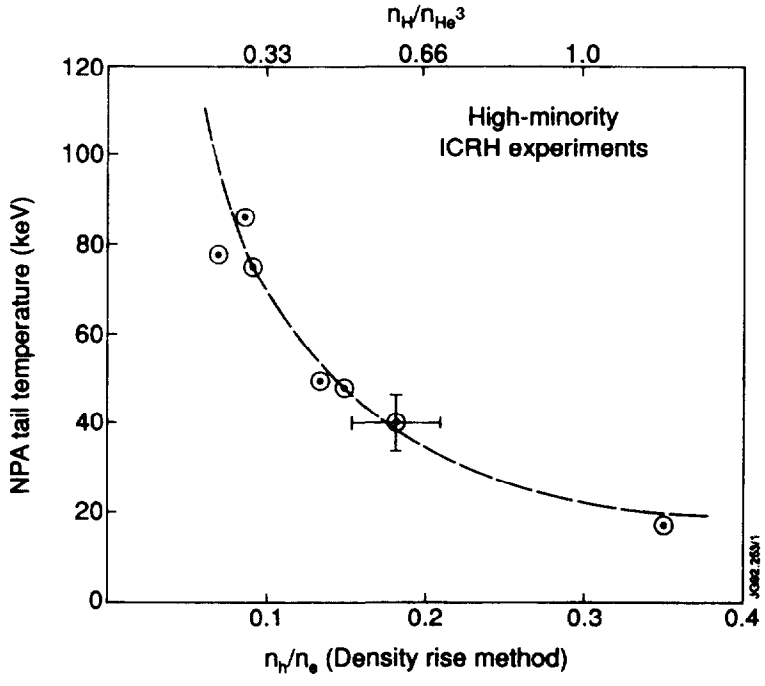

FIG. 13. A plot of the H-minority NPA tail temperature as a function of n_H/n_e for the high-minority heating experiments. The broken line was drawn by fitting to a central point and shows the expected $[n_H/n_e]^{-1}$ dependence.

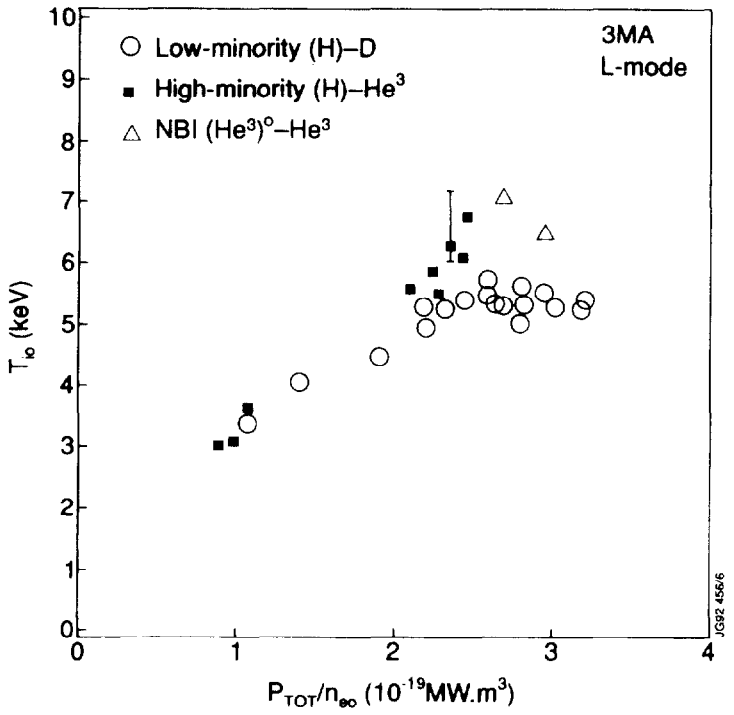

FIG. 14. A plot of the central ion temperature (T_{i0}) as a function of P_{TOT}/n_{e0} during the high minority heating experiments (solid squares) which is compared to the low-minority heating limiter data (open circles). Error bars reflect the corrections due to central burn out of He-like Ni^{27}-line and n_e profile effects. Open triangles are the NBI data points under similar conditions. See Section 5.

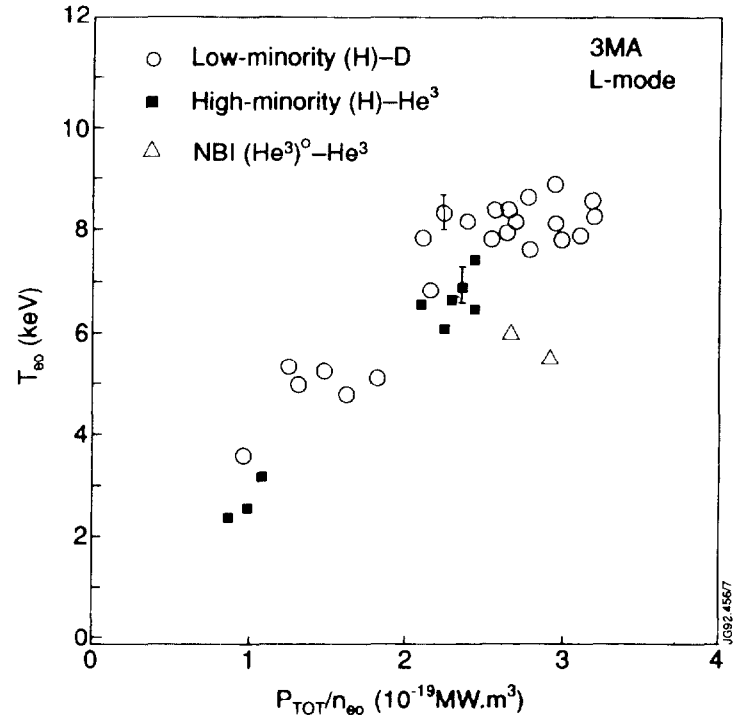

FIG. 15. A plot of the central electron temperature (T_{e0}) as a function of P_{TOT}/n_{e0} during high minority heating experiments (solid squares) which is compared to the low-minority heating limiter data (open circles).

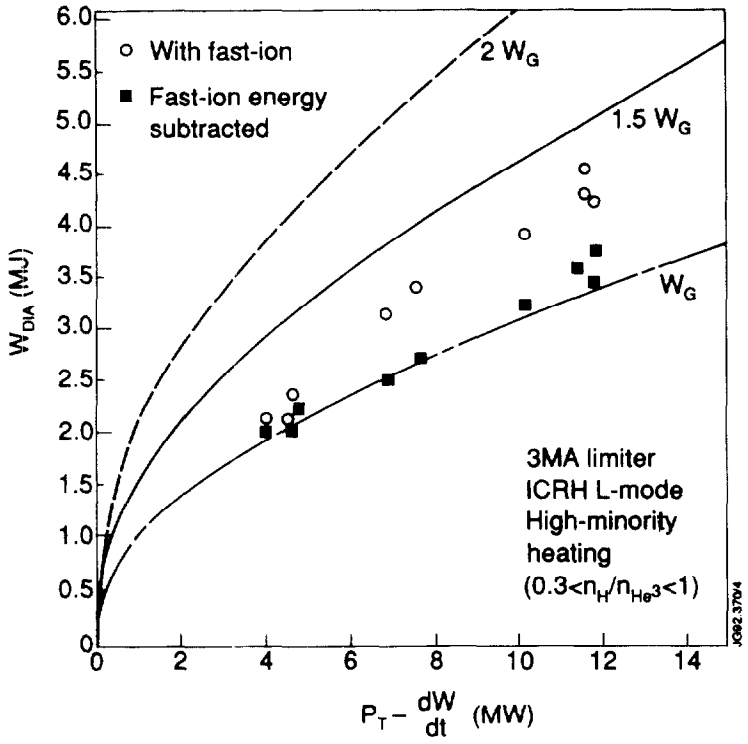

FIG. 16. A plot of the plasma stored energy (diamagnetic loop) as a function of the loss power (P_{TOT}- dW/dt) in the high minority heating experiments. Squares represent the data when the fast-ion energy has been subtracted. Lines drawn represent a multiple of Goldston L-mode prediction (W_G) for such discharges.

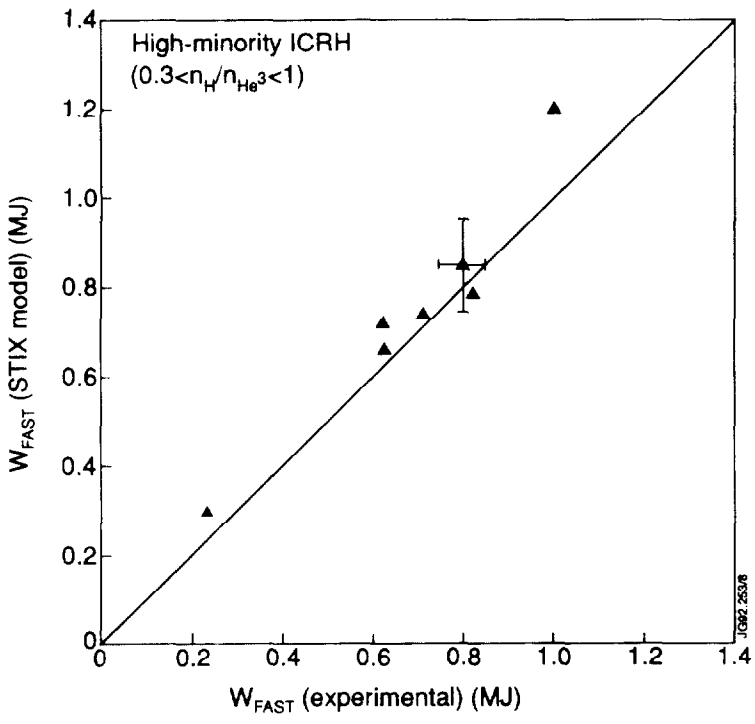

FIG. 17. The minority average energy $<E>$ as calculated from the Stix theory is plotted against the experimentally deduced W_f (see text) for the high minority heating experients. The points should ideally lie along the 45°-line drawn.

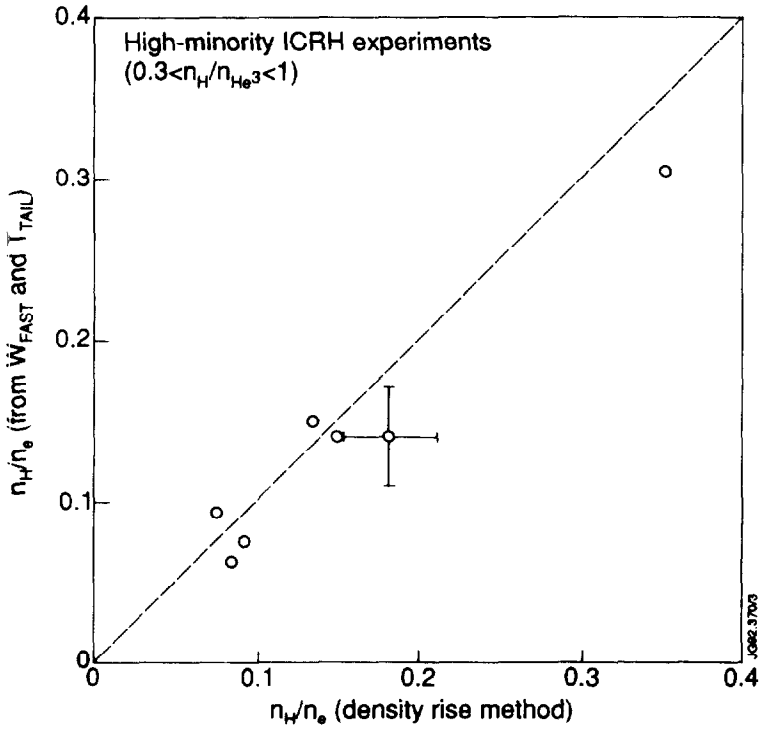

FIG. 18. The minority density deduced from the experimental values of W_f and the measured T_t is plotted against the minority density obtained from the density-rise method for a consistency check. The points should ideally lie along the 45° line drawn.

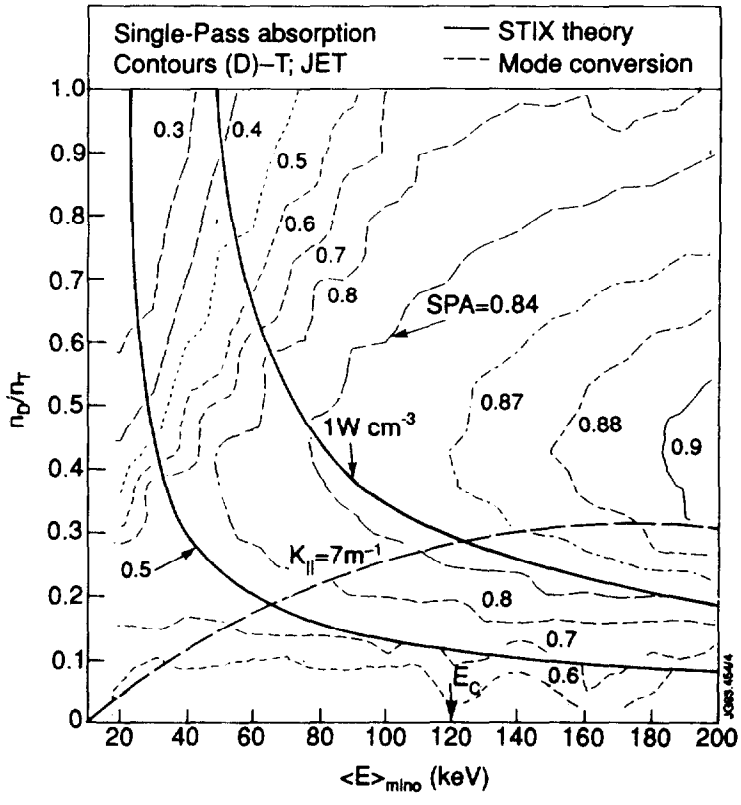

FIG. 19. Single pass absorption contours in a n_D/n_T vs minority $<E>$ diagram in a (D)-T plasma similar to Fig. 6. Other plasma parameters are: $T_e = 8$keV, $n_{e0} = 6 \cdot 10^{19}$m^{-3} and $T_T = 8$keV.

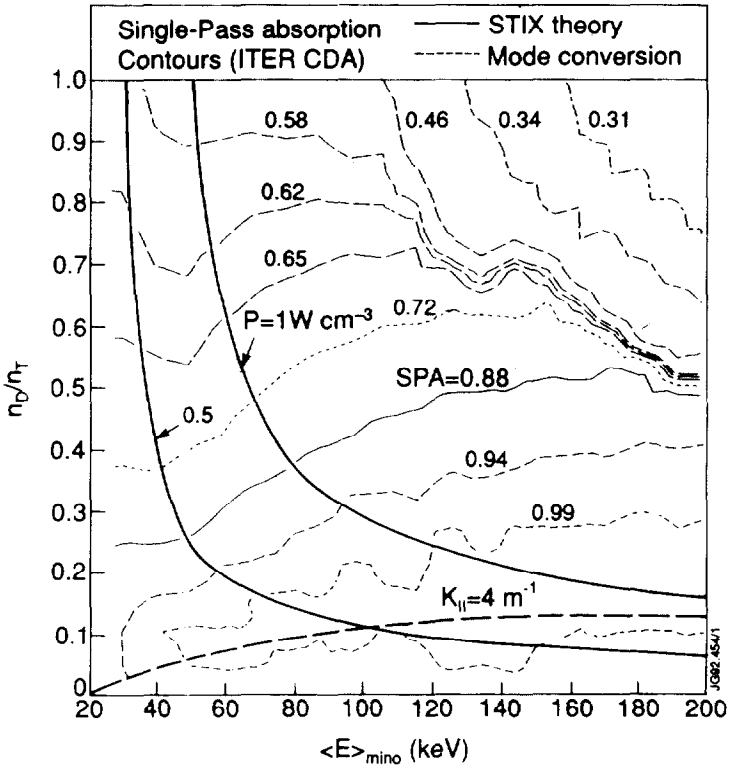

FIG. 20. Single pass absorption contours in a n_D/n_T vs minority $<E>$ diagram in a ITER CDA (Conceptual Design Activity) (D)-T plasma similar to that shown in Fig. 19. Other plasma parameters are: $T_e = 15$keV, $n_{e0} = 9 \bullet 10^{19}$m^{-3} , $T_T = 15$keV, . $R_0 = 6$m, $a_p = 2.2$m, f = 36 MHz and $B_\phi = 4.85$T.

ANNEX

P.-H. REBUT, A. GIBSON, M. HUGUET, J.M. ADAMS[1], B. ALPER, H. ALTMANN, A. ANDERSEN[2], P. ANDREW[3], M. ANGELONE[4], S. ALI-ARSHAD, P. BAIGGER, W. BAILEY, B. BALET, P. BARABASCHI, P. BARKER, R. BARNSLEY[5], M. BARONIAN, D.V. BARTLETT, L. BAYLOR[6], A.C. BELL, G. BENALI, P. BERTOLDI, E. BERTOLINI, V. BHATNAGAR, A.J. BICKLEY, D. BINDER, H. BINDSLEV[2], T. BONICELLI, S.J. BOOTH, G. BOSIA, M. BOTMAN, D. BOUCHER, P. BOUCQUEY, P. BREGER, H. BRELEN, H. BRINKSCHULTE, D. BROOKS, A. BROWN, T. BROWN, M. BRUSATI, S. BRYAN, J. BRZOZOWSKI[7], R. BUCHSE[22], T. BUDD, M. BURES, T. BUSINARO, P. BUTCHER, H. BUTTGEREIT, C. CALDWELL-NICHOLS, D.J. CAMPBELL, P. CARD, G. CELENTANO, C.D. CHALLIS, A.V. CHANKIN[8], A. CHERUBINI, D. CHIRON, J. CHRISTIANSEN, P. CHUILON, R. CLAESEN, S. CLEMENT, E. CLIPSHAM, J.P. COAD, I.H. COFFEY[9], A. COLTON, M. COMISKEY[10], S. CONROY, M. COOKE, D. COOPER, S. COOPER, J.G. CORDEY, W. CORE, G. CORRIGAN, S. CORTI, A.E. COSTLEY, G. COTTRELL, M. COX[11], P. CRIPWELL[12], O. Da COSTA, J. DAVIES, N. DAVIES, H. de BLANK, H. de ESCH, L. de KOCK, E. DEKSNIS, F. DELVART, G.B. DENNE-HINNOV, G. DESCHAMPS, W.J. DICKSON[13], K.J. DIETZ, S.L. DMITRENKO, M. DMITRIEVA[14], J. DOBBING, A. DOGLIO, N. DOLGETTA, S.E. DORLING. P.G. DOYLE, D.F. DÜCHS, H. DUQUENOY, A. EDWARDS, J. EHRENBERG, A. EKEDAHL, T. ELEVANT[7], S.K. ERENTS[11], L.G. ERIKSSON, H. FAJEMIROKUN[12], H. FALTER, J. FREILING[15], F. FREVILLE, C. FROGER, P. FROISSARD, K. FULLARD, M. GADEBERG, A. GALETSAS, T. GALLAGHER, D. GAMBIER, M. GARRIBBA, P. GAZE, R. GIANNELLA, R.D. GILL, A GIRARD, A. GONDHALEKAR, D. GOODALL[11], C. GORMEZANO, N.A. GOTTARDI, C. GOWERS, B.J. GREEN, B. GRIEVSON, R. HAANGE, A. HAIGH, C.J. HANCOCK, P.J. HARBOUR, T. HARTRAMPF, N.C. HAWKES[11], P. HAYNES[11], J.L. HEMMERICH, T. HENDER[11], J. HOEKZEMA, D. HOLLAND, M. HONE, L. HORTON, J. HOW, M. HUART, I. HUGHES, T.P. HUGHES[10], M. HUGON, Y. HUO[16], K. IDA[17], B. INGRAM, M. IRVING, J. JACQUINOT, H. JAECKEL, J.F. JAEGER, G. JANESCHITZ, Z. JANKOVICZ[18], O.N. JARVIS, F. JENSEN, E.M. JONES, H.D. JONES, L.P.D.F. JONES, S. JONES[19], T.T.C. JONES, J.-F. JUNGER, F. JUNIQUE, A. KAYE, B.E. KEEN, M. KEILHACKER, G.J. KELLY, W. KERNER, A. KHUDOLEEV[21], R. KONIG, A. KONSTANTELLOS, M. KOVANEN[20], G. KRAMER[15], P. KUPSCHUS, R. LÄSSER, J.R. LAST, B. LAUNDY, L. LAURO-TARONI, M. LAVEYRY, K. LAWSON[11], M. LENNHOLM, J. LINGERTAT[22], R.N. LITUNOVSKI, A. LOARTE, R. LOBEL, P. LOMAS, M. LOUGHLIN, C. LOWRY, J. LUPO, A.C. MAAS[15], J. MACHUZAK[19], B. MACKLIN, G. MADDISON[11], C.F. MAGGI[23], G. MAGYAR, W. MANDL[22], V. MARCHESE, G. MARCON, F. MARCUS, J. MART, D. MARTIN, E. MARTIN, R. MARTIN-SOLIS[24], P. MASSMANN, G. MATTHEWS, H. McBRYAN, G. McCRACKEN[11], J. McKIVITT, P. MERIGUET, P. MIELE, A. MILLER, J. MILLS, S.F. MILLS, P. MILLWARD, P. MILVERTON, E. MINARDI[4], R. MOHANTI[25], P.L. MONDINO, D. MONTGOMERY[26], A. MONTVAI[27], P. MORGAN, H. MORSI, D. MUIR, G. MURPHY, R. MYRNÄS[28], F. NAVE[29], G. NEWBERT, M. NEWMAN, P. NIELSEN, P. NOLL, W. OBERT, D. O'BRIEN, J. ORCHARD, J. O'ROURKE, R. OSTROM, M. OTTAVIANI, M. PAIN, F. PAOLETTI, S. PAPASTERGIOU, W. PARSONS, D. PASINI, D. PATEL, A. PEACOCK, N. PEACOCK[11], R.J.M. PEARCE, D. PEARSON[12], J.F. PENG[16], R. PEPE DE SILVA, G. PERINIC, C. PERRY, M. PETROV[21], M.A. PICK, J. PLANCOULAINE, J.-P POFFÉ, R. PÖHLCHEN, F. PORCELLI, L. PORTE[13], R. PRENTICE, S. PUPPIN, S. PUTVINSKII[8], G. RADFORD[30], T. RAIMONDI, M.C. RAMOS DE ANDRADE, R. REICHLE, J. REID, S. RICHARDS, E. RIGHI, F. RIMINI, D. ROBINSON[11], A. ROLFE, R.T. ROSS, L. ROSSI, R. RUSS, P. RUTTER, H.C. SACK, G. SADLER, G. SAIBENE, J.L. SALANAVE, G. SANAZZARO, A. SANTAGIUSTINA, R. SARTORI, C. SBORCHIA, P. SCHILD, M. SCHMID, G. SCHMIDT[31], B. SCHUNKE, S.M. SCOTT, L. SERIO, A SIBLEY, R. SIMONINI, A.C.C. SIPS, P. SMEULDERS, R. SMITH, R. STAGG, M. STAMP, P. STANGEBY[3], R. STANKIEWICZ[32], D.F. START, C.A. STEED, D. STORK, P.E. STOTT, P. STUBBERFIELD, D. SUMMERS, H. SUMMERS[13], L. SVENSSON, J.A. TAGLE[33], M. TALBOT, A. TANGA, A. TARONI, C. TERELLA, A TERRINGTON, A TESINI, P.R. THOMAS, E. THOMPSON, K. THOMSEN, F. TIBONE, A. TISCORNIA, P. TREVALION, B. TUBBING, P. VAN BELLE, H. VAN DER BEKEN, G. VLASES, M. VON HELLERMANN, T. WADE, C. WALKER, R. WALTON[31], D. WARD, M.L. WATKINS, N. WATKINS, M.J. WATSON, S. WEBER[34], J. WESSON, T.J. WIJNANDS, J. WILKS, D. WILSON, T. WINKEL, R. WOLF, D. WONG, C. WOODWARD, Y. WU[35], M. WYKES, D. YOUNG, I.D. YOUNG, L. ZANNELLI, A. ZOLFAGHARI[19], W. ZWINGMANN

[1] Harwell Laboratory, UKAEA, Harwell, Didcot, Oxfordshire, UK.
[2] Risø National Laboratory, Roskilde, Denmark.
[3] Institute for Aerospace Studies, University of Toronto, Downsview, Ontario, Canada.
[4] ENEA Frascati Energy Research Centre, Frascati, Rome, Italy.
[5] University of Leicester, Leicester, UK.
[6] Oak Ridge National Laboratory, Oak Ridge, TN, USA.
[7] Royal Institute of Technology, Stockholm, Sweden.
[8] I.V. Kurchatov Institute of Atomic Energy, Moscow, Russian Federation.
[9] Queens University, Belfast, UK.
[10] University of Essex, Colchester, UK.
[11] Culham Laboratory, UKAEA, Abingdon, Oxfordshire, UK.
[12] Imperial College of Science, Technology and Medicine, University of London, London, UK.
[13] University of Strathclyde, Glasgow, UK.
[14] Keldysh Institute of Applied Mathematics, Moscow, Russian Federation.
[15] FOM-Institute for Plasma Physics "Rijnhuizen", Nieuwegein, Netherlands.
[16] Institute of Plasma Physics, Academia Sinica, Hefei, Anhui Province, China.
[17] National Institute for Fusion Science, Nagoya, Japan.
[18] Soltan Institute for Nuclear Studies, Otwock/Świerk, Poland.
[19] Plasma Fusion Center, Massachusetts Institute of Technology, Boston, MA, USA.
[20] Nuclear Engineering Laboratory, Lappeenranta University, Finland.
[21] A.F. Ioffe Physico-Technical Institute, St. Petersburg, Russian Federation.
[22] Max-Planck-Institut für Plasmaphysik, Garching, Germany.
[23] Department of Physics, University of Milan, Milan, Italy.
[24] Universidad Complutense de Madrid, Madrid, Spain.
[25] North Carolina State University, Raleigh, NC, USA.
[26] Dartmouth College, Hanover, NH, USA.
[27] Central Research Institute for Physics, Budapest, Hungary.
[28] University of Lund, Lund, Sweden.
[29] Laboratorio Nacional de Engenharia e Tecnologia Industrial, Sacavem, Portugal.
[30] Institute of Mathematics, University of Oxford, Oxford, UK.
[31] Princeton Plasma Physics Laboratory, Princeton University, Princeton, NJ, USA.
[32] RCC Cyfronet, Otwock/Świerk, Poland,
[33] Centro de Investigaciones Energéticas, Medioambientales y Tecnológicas, Madrid, Spain.
[34] Freie Universität, Berlin, Germany.
[35] Insitute for Mechanics, Academia Sinica, Beijing, China.